

# Roll Stall for Low-Aspect-Ratio Wings

Matt Shields\* and Kamran Mohseni†  
University of Florida, Gainesville, Florida 32611-6250

DOI: 10.2514/1.C031933

The longitudinal aerodynamics of micro aerial vehicles, although not fully understood, have been the subject of several studies in recent years; however, little work has been done to investigate the lateral loading. In this experiment, flat-plate wings with rectangular planforms of aspect ratios  $AR = 0.75, 1, 1.5,$  and  $3$  and tapered planforms of  $\lambda = 0.75, 0.5,$  and  $0.25$  were placed in the wind tunnel at a Reynolds numbers of  $7.5 \times 10^4$ . Angle-of-attack sweeps were performed at sideslip angles of  $\beta = 0, -5, -10, -15, 20$  and  $-35$  deg, and the side force, yaw moment, and roll moment were measured. Although the side force and yaw moment coefficients ( $C_{SF}$  and  $C_n$ ) were typically negligible, the roll moment coefficient  $C_l$  was found to increase linearly with angle of attack before stalling in a manner reminiscent of a lift curve. This “roll stall”, which has not previously been observed for micro-aerial-vehicle-type wings, is attributed to the upstream tip vortex creating an additional lift component due to its impact on the spanwise variation of effective angle of attack in addition to the force generated by its own low-pressure core. As the downstream tip vortex is convected away from the wing, a net moment is created. Computations of the roll-stability derivative indicate that a micro aerial vehicle in equilibrium flight conditions may experience magnitudes of  $C_{l,\beta}$  at the upper limit of, or even above, the range of  $-0.10 \leq C_{l,\beta} \leq 0$  considered to represent good handling qualities in aircraft.

## Nomenclature

AR	=	aspect ratio
$b$	=	wing span, cm
$c$	=	chord, cm
$C_L$	=	lift coefficient
$C_{L_{\max}}$	=	maximum lift coefficient (at stall)
$C_{SF}$	=	side force coefficient
$C_l$	=	roll moment coefficient
$C_{l,\beta}$	=	roll-stability derivative, $\text{rad}^{-1}$
$C_n$	=	yaw moment coefficient
$C_{n,\beta}$	=	yaw stiffness derivative, $\text{rad}^{-1}$
$f_s$	=	data-sampling frequency, Hz
$Re$	=	Reynolds number
$U_0$	=	freestream velocity, m/s
$x_b, y_b, z_b$	=	body-centered axes
$\alpha$	=	angle of attack, deg
$\alpha_{\text{stall}}$	=	stall angle of attack, deg
$\beta$	=	sideslip angle, deg
$\lambda$	=	taper ratio
$\phi$	=	bank angle, deg

## I. Introduction

IN RECENT years, the capabilities of micro aerial vehicles (MAVs) have improved so dramatically that several different institutions have designed and flown a wide variety of vehicles for a multitude of applications [1–5]. These designs typically rely heavily on iterative testing procedures because no readily accessible analytic tools are available for MAV development. At the core of the issue is the difficulty in modeling the aerodynamic loads and associated stability derivatives of low-aspect-ratio (LAR) flyers at low Reynolds

numbers, which are characterized by three-dimensional flow phenomena dominating the flow over much of the wing. The viscous effects of the flowfield cause significant departures from inviscid approximations for aerodynamic loading [6] and create several forms of flow phenomena. The Reynolds number range typically associated with MAVs, between  $10^4$  and  $10^5$ , promotes the development of a laminar separation bubble (LSB) in which the separated flow over the suction surface can entrain enough external fluid to increase pressure and reattach to the wing surface [7,8]. The LSB affects the surface pressure distribution, the stall characteristics, and the unsteady nature of the flow downstream of the bubble [7,9,10].

A phenomenon similar to the separation bubble is the leading-edge vortex (LEV). Usually associated with slender delta wings at supersonic speeds or flapping wings at lower Reynolds numbers, the LEV is created by the roll-up of the shear layer at a sharp leading edge and is stabilized by the strong spanwise flow through the core, which acts as a sink of vorticity [11–15]. A weak LEV has also been observed to form on nonslender delta wings at moderate Reynolds numbers in the MAV regime, although it tends to be susceptible to early bursting due to the strong adverse pressure gradient [16]. Although the swept leading edge promotes a more stable vortex, a rectangular planform typically does not allow the LEV to remain attached to the wing [17,18]. The LEV contains a high-velocity, low-pressure inner core, which is known to locally augment the lift [12,19,20].

A final flow phenomenon known to affect the aerodynamics of MAVs is the tip vortex created by the pressure difference between the suction side and the pressure side of the wing. The short wingspan of LAR flyers allows the influence of the tip vortex to propagate over a majority of the lifting surface and acts to keep the flow attached at high angles of attack, increasing the stall angle and  $C_{L_{\max}}$  [21–23]. In addition, the tip vortices are known to interact strongly with the LEV at low aspect ratios as the downwash keeps the shed LEV near the suction surface [14]. The strength of tip vortices can develop asymmetrically at increased angles of attack and bank; in addition, the low-pressure cores of the vortices can wander asymmetrically, resulting in roll and yaw moments [24–27].

The flow phenomena associated with LAR wings at low Reynolds numbers have been investigated for years; some of the first investigations of LAR wings took place in the early 20th century [28,29], although it is only recently that their impact on MAVs has been considered. The majority of the available literature focuses on measuring the lift, drag, and pitching moment of flat-plate wings and airfoils (see, for example, [9] or [30]). An advantage of the experimental setup in this investigation is the ability to actuate a model in multiple degrees of freedom in addition to being able to

Presented as Paper 2012-4462 at the AIAA Guidance, Navigation and Control Conference, Minneapolis, MN, 12–16 August 2012; received 24 April 2012; revision received 19 October 2012; accepted for publication 23 October 2012; published online 2 May 2013. Copyright © 2012 by the American Institute of Aeronautics and Astronautics, Inc. All rights reserved. Copies of this paper may be made for personal or internal use, on condition that the copier pay the \$10.00 per-copy fee to the Copyright Clearance Center, Inc., 222 Rosewood Drive, Danvers, MA 01923; include the code 1542-3868/13 and \$10.00 in correspondence with the CCC.

\*Graduate Research Assistant, Mechanical & Aerospace Engineering Department. Student Member AIAA.

†William P. Bushnell Endowed Chair in Mechanical & Aerospace Engineering Department and Electrical & Computer Engineering Department, Institute for Networked Autonomous Systems. Associate Fellow AIAA.

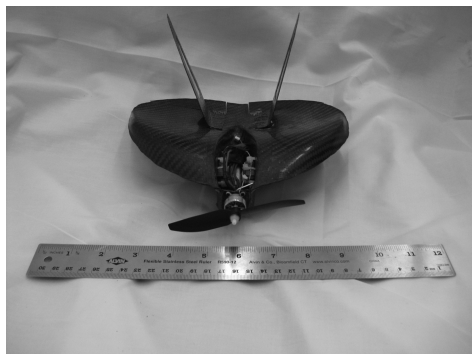


Fig. 1 PIPER MAV developed by the group; photo from December 2008.

measure all six aerodynamic load components, capabilities that are not typical to most wind tunnels. Because of this, minimal results exist for the lateral loads of LAR wings. The authors' experience with MAV design and flight testing indicates that achieving lateral directional stability is one of the more challenging aspects of developing a reliable vehicle. The PIPER MAV, shown in Fig. 1, is a reliable platform capable of 10 min flights using radio controls. Earlier iterations of this vehicle, however, were notoriously susceptible to lateral instabilities, which could unexpectedly cause rapid roll oscillations ("jitters") and occasionally unrecoverable rolls. It is thus important to investigate the lateral loading of low-aspect-ratio wings at low Reynolds numbers to determine the influence of the unique flow conditions on the aerodynamic stability of MAVs.

The outline of this paper is as follows. The experimental setup, testing procedure, and data-acquisition methods are described in Sec. II. Flow visualization and force balance measurements are presented and analyzed in Sec. III. Estimates of relevant stability derivatives and their impact on the control of MAVs are considered in Sec. IV. Finally, the major results and implications of the paper are summarized in Sec. V.

## II. Experimental Setup

### A. Wind Tunnel and Force Balance

All testing conducted in the course of this investigation used the Prototunnel located at the University of Florida. The Prototunnel and its associated infrastructure have been described in detail in a previous publication by the authors [23]. To briefly summarize the key features of the setup, the  $0.35 \times 0.35$  m test section is outfitted with a model-positioning system (MPS), which can actuate a model in roll, pitch, yaw, and plunge; a diagram of the MPS can be seen in Fig. 2. The MPS allows accurate positioning of the model to within  $\pm 0.1$  deg in angle of attack and  $\pm 0.5$  deg in sideslip. Forces and moments are measured by the microloading technology (MLT) balance, a six-component internal balance designed for MAV-scale loads. Previous publications by the authors have described the calibration of the balance [23,31]; additional calibrations were undertaken for the lateral directional axes for this investigation and are discussed in Sec. II.D.

It is important to define the coordinate system used for the investigation. Because the eventual goal of the research is MAV stability and control, it is logical to present the results in the body axes of the model; thus, the side force discussed in this paper is defined as positive toward the right wing tip. It differs from the so-called cross-wind force sometimes reported in wind-tunnel testing, which is orthogonal to the lift and drag vectors. Sideslip angle is defined as negative if there is a component of the flow velocity vector in the direction of the  $+y_b$  axis because this corresponds to the wing translating in a positive flight direction [32]. The relevant coordinate axes and directions of positive lateral forces and moments are shown in Fig. 3.

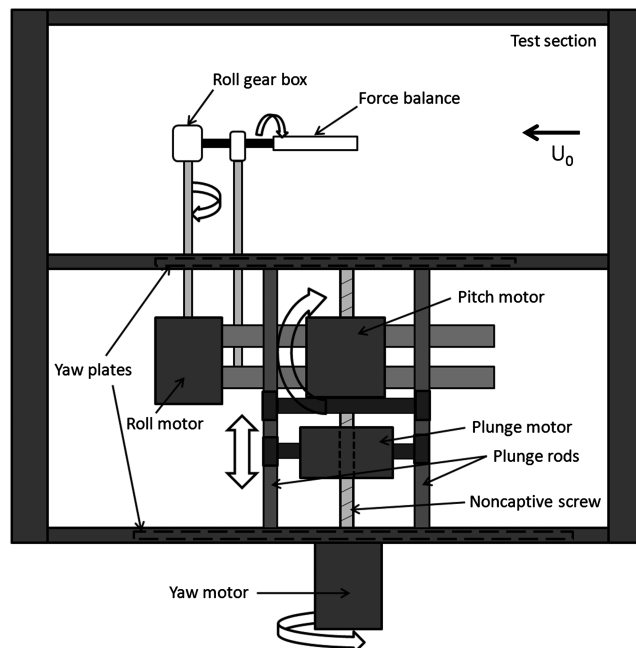


Fig. 2 MPS mounted under the test section. Block arrows indicate available degrees of freedom that can be actuated by each motor (figure not to scale).

### B. Models and Testing Procedure

Flat-plate wings (0% camber) that have previously been tested by the authors were used again in this investigation. The models have a 5:1 elliptically rounded leading edge and thickness-to-root-chord ratios between 2.4 and 5.4%. The dimensions of these models are listed in Table 1. The desired data from the experiment consisted of the sample mean of the roll moment, yaw moment, and side force at a given incidence angle of attack and sideslip. To compute this, a "zero reference data set" is first obtained with the wind off at each position and is subsequently subtracted from the wind-on aerodynamic loads to eliminate the inertial forces of the model. For the sideslip angles tested between  $\beta = 0$  and  $-35$  deg, side force, yaw moment, and roll moment data were collected at angles of attack between  $-24 < \alpha < 45$  deg; selected cases (such as the  $AR = 3$  model) were only tested up to  $\alpha = 40$  deg because this was the angle of attack at which lift stall occurs [23]. Only negative sideslip angles were tested, thus inherently assuming symmetric results about  $\beta = 0$  deg. Several test cases were repeated at a full range of positive and negative sideslip angles, and it was found that the measured results were indeed symmetric, justifying this assumption.

### C. Data Acquisition

At each data collection point,  $2^{14}$  samples were simultaneously collected for all six channels at a sampling rate of  $f_s = 2^{12}$  Hz; the 4 s sampling period was deemed sufficient for any unsteady flow phenomena to be averaged out over the sample time [14,24,33]. A low-pass fourth-order Butterworth filter set at 1 kHz was used to

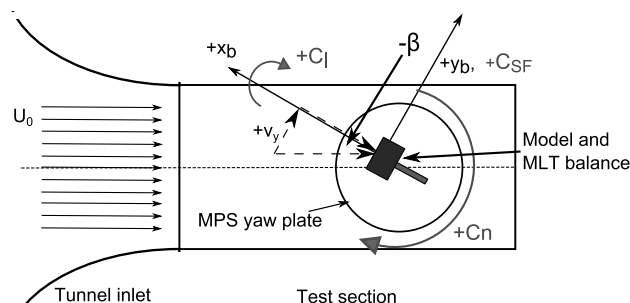


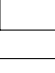

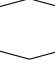
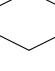
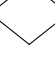


Fig. 3 Coordinate axes and definition of sideslip angle.

**Table 1 Test-model dimensions**

AR	$c_{\text{root}}$ , cm	$c_{\text{tip}}$ , cm	$b$ , cm	$\lambda$	Diagram
<i>Rectangular planforms</i>					
0.75	16.9	16.9	12.7	1	
1	15.2	15.2	15.2	1	
1.5	10.2	10.2	15.2	1	
3	7.6	7.6	22.9	1	
<i>Tapered planforms</i>					
1	15.2	11.4	15.2	0.75	
1	15.2	7.6	15.2	0.5	
1	15.2	3.8	15.2	0.25	

eliminate high-frequency noise, which was aliased into the sampling bandwidth. The strain-gauge data were converted to physical loads using an iterative technique based on the AIAA strain-gauge standard [34]. All results were also corrected for solid blockage, wake blockage, and streamline curvature based on the techniques presented by Rae and Pope [35]; minimal blockage effects were observed due to the small thickness of the models tested.

#### D. Error and Uncertainty

Error analysis performed on the data collected in this experiment was based on techniques presented by Bendat and Piersol [36]. Because only the steady-state loads were of interest, the desired results from the data collected at each incidence angle merely required computing the sample mean. The running average of the first two moments of data collected at low to moderate angles of attack were seen to converge within approximately 1000 samples for all measured channels, indicating good stationarity. At high angles of attack corresponding to the roll stall regime (typically above  $\alpha = 15$  deg, to be discussed further in Sec. III), noticeable deviations between test runs were observed at low sideslip angles. This indicates that the stalled flow regime creates an unsteady flow environment not well modeled by the quasi-steady experiment; however, the focus of this investigation is the loading in the flight envelope of MAVs in which the data were repeatable with no discernible deviation between test runs. It is sufficient to identify the unsteady region as a problematic flight environment for a LAR aircraft.

The errors associated with the measurements include bias, random, and quantization errors. Bias errors were estimated by statically loading the MLT balance with weights corresponding to the magnitude of experimentally measured loads. Relative to the sample mean, side force and yaw moment show 0.1% error, and roll moment shows 3% error in the range of expected loads for this investigation. Random error and quantization error were negligible due to the large number of samples taken at each data point and the 16-bit resolution of the A/D converter [36]. In addition, 95% confidence intervals were computed for each value of the sample mean. Each data sweep showed confidence bounds of less than 1% of the sample mean with one exception; a given geometry displays a single yaw moment data point (typically at negative angles of attack) corresponding to an increase in the confidence bound to 5–10% of the sample mean. This was caused by increased amplitude fluctuations of the measured data at that point; the larger standard deviation about the mean expands the

95% confidence interval. It is surmised that the tip vortex-shedding frequency at this incidence angle is close to the resonant frequency of the MPS (which varies slightly with model configuration and sideslip angle), and thus the reduced accuracy is due to the vibration of the system. It should be noted that the moments still converge, and the measured loads are repeatable in successive experiments, indicating the validity of the data point.

### III. Results

To quantitatively assess the impact of LAR flow behavior on lateral loading, a series of wind-tunnel tests were conducted using the rectangular and tapered flat-plate wings defined in Table 1. The rectangular wings had aspect ratios of 0.75, 1, 1.5, and 3; the tapered wings had taper ratios of 0.25, 0.5, and 0.75 defined by  $\lambda = c_{\text{tip}}/c_{\text{root}}$ . Tests were conducted at a chord-based Reynolds number of  $7.5 \times 10^4$ ; previous investigations have shown that no significant changes are noticeable in aerodynamic loading between Reynolds numbers of  $5 \times 10^4$  and  $1 \times 10^5$  [22,23], indicating that these results are applicable to the flight regime of MAVs. The lateral loads measured using the MLT balance were the side force, yaw moment, and roll moment, which were nondimensionalized using the dynamic pressure, wing area, and (for the latter two) the wingspan. Sideslip angles of  $\beta = 0, -5, -10, -15, -20,$  and  $35$  deg were measured; the exception was that the AR = 3 model could not be tested at the highest sideslip angle because the longer span infringes upon the boundary layer of the test section.

#### A. Smoke-Wire Visualization

To determine the behavior of the flow around a wing in sideslip, smoke-wire visualization was conducted for all models used in the investigation. A Phantom v210 high-speed camera was mounted above the test section and used to capture the images of the three-dimensional flow around the wing tips. The smoke wire was situated immediately below the leading edge to focus on the structure of the tip vortices instead of the leading-edge separation; for the tapered wing cases, it was placed just below the upstream wing-tip vertex. Results are shown in Figs. 4 and 5.

The most important point to note from the smoke-wire results is the behavior of the tip vortices at increasing sideslip angles. As seen in Fig. 4b, for example, the tip vortex on the upstream (left) wing tip propagates over the surface of the wing in a coherent vortical shape. The downstream (right) tip vortex is convected away from the wing by the freestream flow; this effect is more pronounced at a sideslip angle of  $\beta = -20$  deg, as seen in Fig. 4c. When the angle of attack is increased from  $\alpha = 10$  to  $30$  deg, the propagation over the wing is somewhat similar for each sideslip case, although the structure of the vortex is now disrupted by the increasing adverse pressure gradient. Spanwise flow from left to right still exists, although no coherent vortical structure is visible. The tapered wing in sideslip shown in Fig. 5 also exhibits the tip vortex asymmetry and the disrupted structure at higher angles of attack. By comparing Figs. 4c and 5c, it is clear that the tapered geometry leaves little surface area downstream of the wing tip to be affected by the attached tip vortex and will therefore be less affected by the tip vortex asymmetry than the rectangular wings.

#### B. Roll Moment for Rectangular Wings

The roll moments measured for rectangular flat-plate wings at increasing sideslip angles are displayed in Fig. 6. One of the first points to note is how the shape of the plots for aspect ratios up to 1.5 looks qualitatively similar to a lift polar, manifested by a linear slope at low angles of attack leading to a distinct stall region. This behavior (hereafter referred to as roll stall) is not a well known phenomena; the authors are not aware of any similar experimental results for LAR wings at low Reynolds numbers. The physical explanation for this result is attributed to the presence of the tip vortex, particularly on the upstream wing tip when the wing yaws. It is clear from Fig. 4 that the core of the upstream tip vortex is located above the surface of the sideslipping wing, while the downstream tip vortex has little effect on

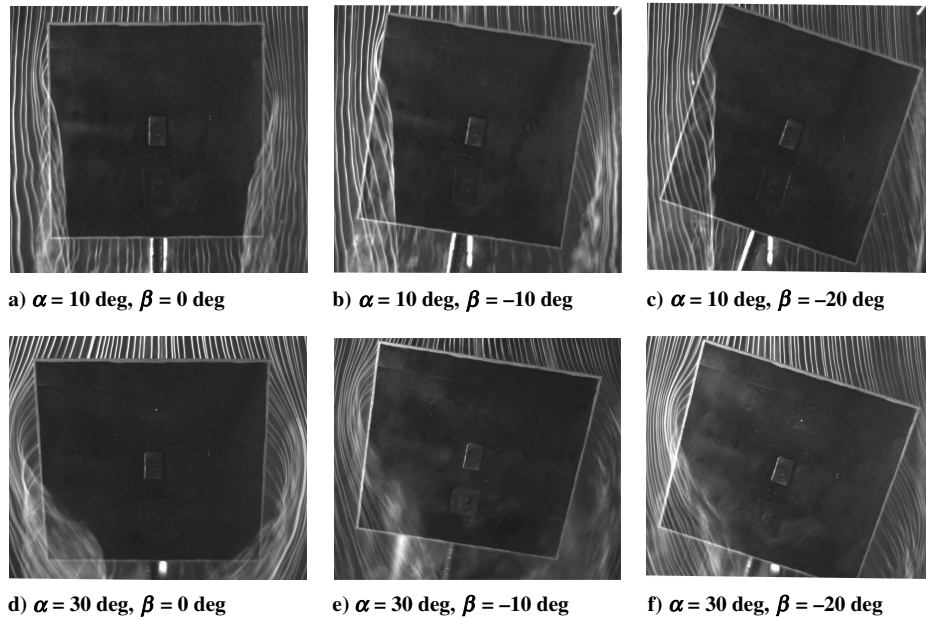


Fig. 4 Smoke-wire visualization for a flat-plate wing with  $AR = 1$  at  $\alpha = 10$  and  $30$  deg and increasing sideslip angles for  $Re = 7.5 \times 10^4$ .

the flow above the test model; this condition is unique to LAR wings. The induced velocities created by the upstream vortex at a chordwise station on the wing can be computed using the Biot–Savart law and a qualitative example is shown in Fig. 7. This schematic shows how an upwash is actually created near the wing tip while the rest of the wing experiences a downwash, resulting in an increased effective angle of attack near the tip and decreased incidence angles elsewhere. The proportional spanwise variation in sectional lift creates a positive rolling moment.

In addition to the effects of the tip vortex asymmetry on the spanwise loading of the wing, at increasing sideslip angles and angles of attack, the separated shear layer at the upstream edge will experience greater velocity gradients and a correspondingly greater strength of the rolled-up vortex [27]. The low-pressure core acts to locally augment the lift on the upstream (left) wing tip; because there is no corresponding downstream tip vortex above the surface of the wing to balance this force, an additional component of positive roll moment is induced. At higher angles of attack, the stronger adverse pressure gradient disrupts the coherent nature of the tip vortex, as

seen in Fig. 4f. This can be considered similar to vortex breakdown in delta wings [13,37]. The reduced strength of the tip vortex decreases its impact on the induced angle of attack and the local pressure augmentation, corresponding to the roll stall seen in Fig. 6.

Although the results shown in Figs. 6a–6c are qualitatively similar, the higher-aspect-ratio case in Fig. 6d displays a more nonlinear roll moment slope. This is unlike the lift performance of LAR wings, in which higher aspect ratios exhibit a more linear slope and aspect ratios near unity are noticeably nonlinear [21–23]. At low angles of attack, the higher-aspect-ratio wing experiences a more conventional aerodynamic loading (i.e., dominated by the bound circulation of the wing), which ideally should not create a significant roll moment at any sideslip angle for a thin wing [32,38]. At low  $\alpha$ , the slope of the roll moment polar is nonzero but small for any sideslip case except  $\beta = 0$  deg and is then observed to at least triple in magnitude above  $\alpha = 10$  deg. At these higher angles of attack, the flow separation is more pronounced, and the influence of the tip vortex is more prevalent; as a result, the roll moment behaves more similarly to the lower-aspect-ratio cases. It should be noted that wings with aspect

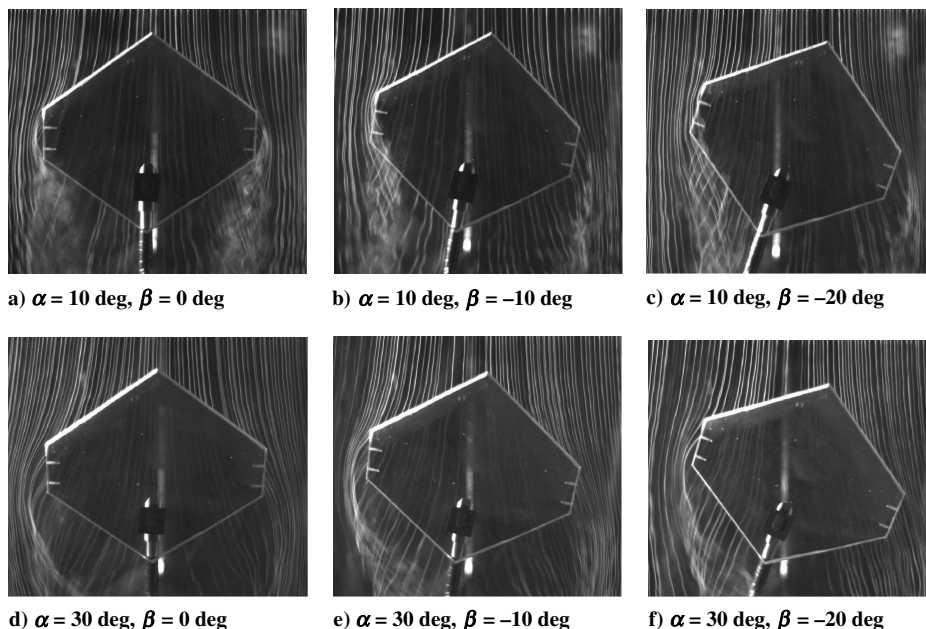


Fig. 5 Smoke-wire visualization for a flat-plate wing with  $AR = 1$  and  $\lambda = 0.25$  at  $\alpha = 10$  and  $30$  deg and increasing sideslip angles for  $Re = 7.5 \times 10^4$ .

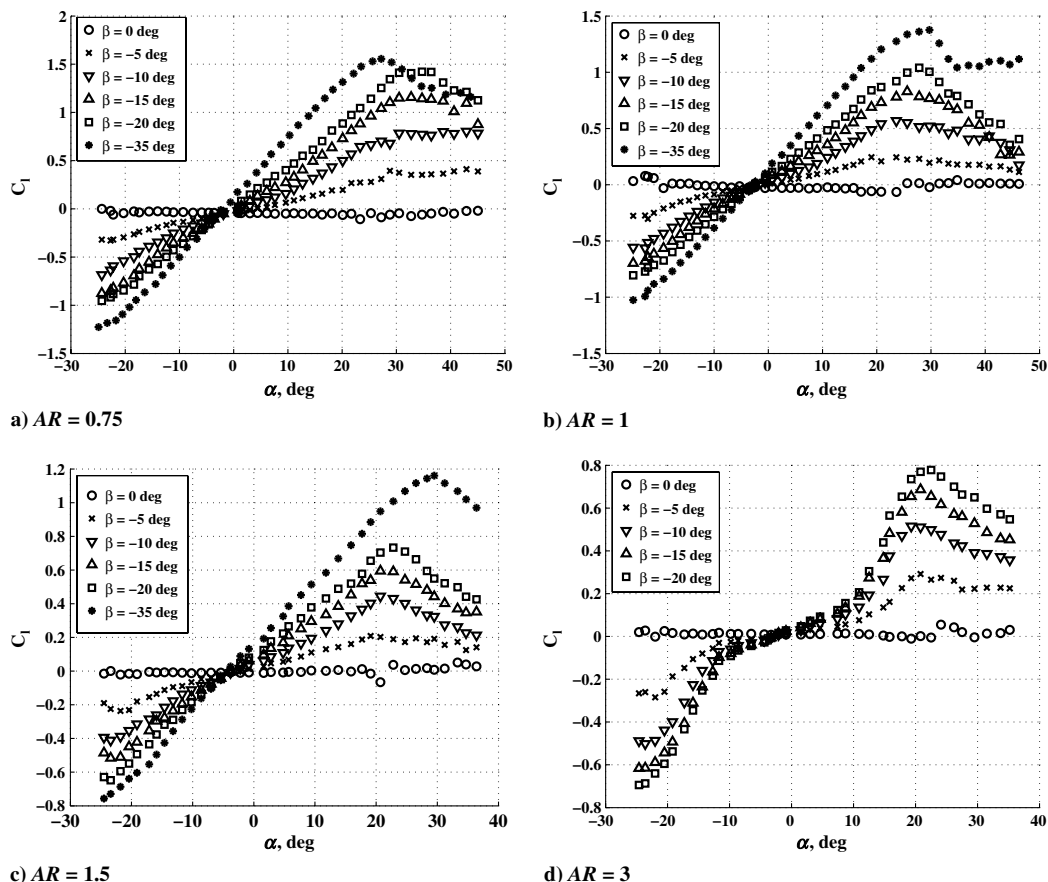


Fig. 6 Roll moment coefficient for rectangular flat-plate wings in sideslip at  $Re = 7.5 \times 10^4$ .

ratios between 2 and 3 have traditionally been considered an intermediate aspect ratio [39]; tip effects have more impact than they do for a conventional aircraft wing ( $AR \gg 3$ ), but there is significantly less interaction between the tip vortices and the LEV than there is for a LAR wing that is more typical of MAV planforms ( $AR \sim 1$ ). The  $AR = 3$  case thus displays some similarities to a conventional wing (as seen with the small magnitude of the roll moments for  $\alpha < 10$  deg) as well as a lower-aspect-ratio wing (manifested by the significant increase in  $C_l$  for  $\alpha > 10$  deg).

### C. Roll Moment for Tapered Wings

To investigate the effects of leading-edge geometry, a series of tapered wings were tested at the same angles of attack and sideslip as the rectangular wings. Because the aspect ratio of all tapered wings (based on the midchord span) is equal to unity, the  $AR = 1$  results from Fig. 6b are included to provide a baseline reference. The results are shown in Fig. 8. In several ways, the results are similar to those of

the rectangular planforms. It is clear that increasing the sideslip angle results in a greater value of the rolling moment; although this can be mainly attributed to the presence of the tip vortex, it is also important to note that, for lower values of the taper ratio, an increased amount of spanwise flow is fed into the developing tip vortex by the LEV [14]. This vorticity-sink mechanism helps to strengthen the tip vortex and improves its ability to withstand an adverse pressure gradient. This trend is noticeable in Fig. 8; for  $\lambda = 1$  and 0.75, roll stall occurs between 20 and 30 deg in both cases, but the post-stall gradient is much more gentle for the tapered wing, indicating that the disruption of the upstream tip vortex is less drastic than for rectangular wings.

Decreasing the taper ratio to 0.5 prevents roll stall from occurring, although the slope does decrease around  $\alpha = 20$  deg, as seen in Fig. 8c. This suggests that the  $\lambda = 0.5$  case is more effective at feeding vorticity from the LEV into the tip vortex at higher angles of attack than the higher taper ratio cases, resulting in a more coherent tip vortex that can withstand breakdown better than on a rectangular wing. When the taper ratio is decreased to 0.25 (i.e., smallest wing tips), the magnitude of the roll moment is significantly decreased after remaining relatively constant over the previous plots. This can be attributed to the small wing tip only allowing a limited chordwise development of the tip vortex. The geometry of the  $\lambda = 0.25$  wing has the least surface area downstream of the wing tip, and thus the aforementioned effects of the tip vortex's induced velocity are minimized. In addition, the wing does appear to experience roll stall around  $\alpha = 20$  deg, unlike the  $\lambda = 0.5$  case; however, there is a substantial recovery zone where the roll moment increases to a value greater than the stall value. This may represent the angle of attack where the formation of the LEV weakens and does not contribute much to the strength of the tip vortex; the nominally constant value of roll moment seen at higher angles is purely due to the roll-up of the shear layer over the wing tip.

In the course of the experiment, it was observed that the roll moment of a wing with zero sideslip was not necessarily zero, as

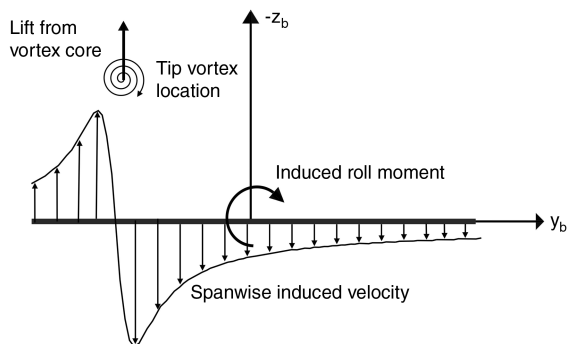


Fig. 7 Illustration of the roll moment generated by the upstream tip vortex via the induced spanwise velocity profile (computed using the Biot-Savart law) and the lift from the vortex core.

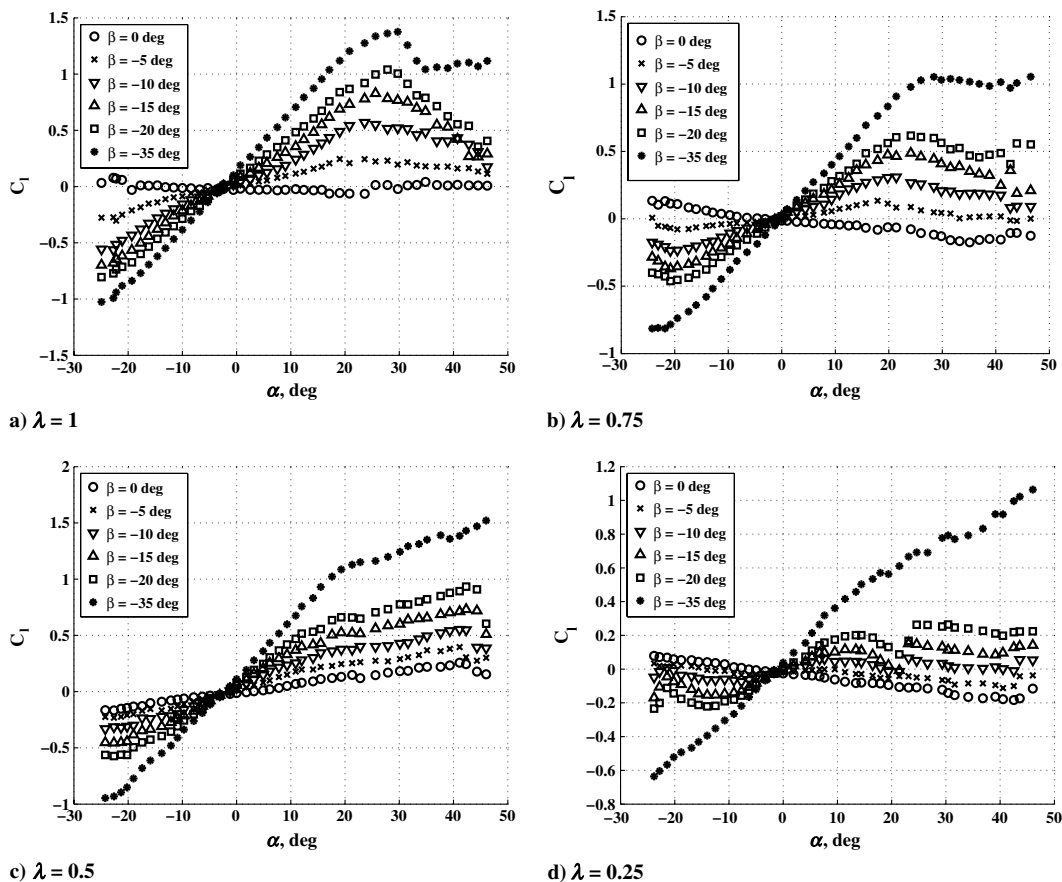


Fig. 8 Roll moment coefficient for tapered flat-plate wings with  $AR = 1$  in sideslip at  $Re = 7.5 \times 10^4$ .

would be expected for a wing with identical tip vortices; this is slightly noticeable in Fig. 6 and is more prominent for the tapered wing cases in Fig. 8. In addition, the wings with the aspect ratio of unity were highly susceptible to deviations in roll moment due to slight perturbations in sideslip about the baseline condition of zero. To illustrate this, the square wing with  $AR = 1$  was swept through the usual range of angles of attack at sideslip angles incrementally above and below zero; the results for the roll moment are shown in Fig. 9. At an approximately zero angle of sideslip, neither tip vortex should be completely swept away from the wing to create the lateral asymmetry experienced by the same wing in high sideslip, and thus no roll moment should be produced. From the data in Fig. 9, it is clear that a roll moment is created with negligible sideslip perturbations, and that the gradient of this curve is dependent on the sign of the sideslip angle.

It is also noticeable that the slopes of  $C_l$  versus  $\alpha$  are not perfectly symmetric for  $\beta \rightarrow 0^-$  and  $0^+$ ; this would imply that slightly different

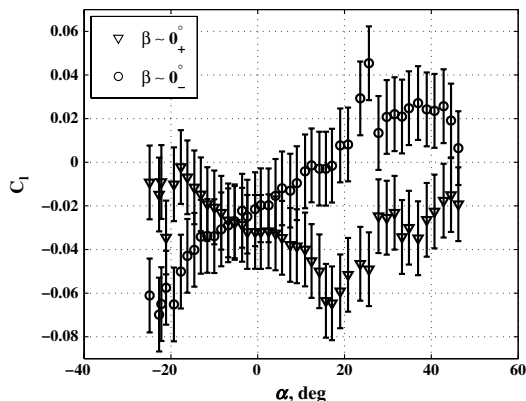


Fig. 9 Roll moment coefficient ( $C_l$ ) with error bars for an  $AR = 1$  flat-plate wing at near-zero sideslip angles at  $Re = 7.5 \times 10^4$ .

stability derivatives would need to be computed for positive or negative sideslip perturbations about  $\beta = 0$  deg. However, when error bars (corresponding to the minimum resolvable roll moment, which yields less than 5% bias error) are added, it can be seen in Fig. 9 that the small variations in the gradient of  $C_l$  near  $\beta = 0$  deg are well within the bounds of the MLT balance's resolution. Hence, these asymmetries can be attributed to experimental uncertainty and the assumption of symmetry about  $\beta = 0$  deg remains valid. There is a small offset in roll moment at zero sideslip ( $C_l \sim -0.025$ ), but because the stability derivatives are computed from the slope of the  $C_l$  versus  $\beta$  curve, this will not affect the computation of the roll-stability derivative.

Although the nonzero roll moment at  $\beta = 0$  deg can be partially attributed to experimental uncertainties in sideslip angle, imperfections in leading-edge geometry and a developing asymmetry of the tip vortices also lead to an unbalanced flowfield on the suction surface of the wing. The influence of the tip vortices can cause a significant variation in laminar separation on airfoils, moving the point of detachment as far back as  $x/c = 60\%$  for  $AR = 2$  at angles of attack as low as  $\alpha = 3$  deg [40]; at the lower aspect ratios investigated here, this influence is even more pronounced. In addition, Gresham et al. [26] observed that LAR wings experience nonzero trim bank angles at zero sideslip due to the uneven development of tip vortices, occasionally requiring angles up to  $\phi = 15$  deg to achieve zero roll moment at low angles of attack. This was attributed to the rounded leading edge of the flat-plate models tested because there is not a uniform separation point on the leading edge; a beveled leading edge was used to bring the trim angle closer to zero. The disparity between the development of the leading-edge vortices on the left and right sides of the wing, which in turn influences the strength of the respective tip vortices, greatly impacts the roll moment of tapered wings at zero sideslip, as seen in Fig. 8. It should be noted that the different taper ratios exhibit both positive ( $\lambda = 0.5$ ) and negative ( $\lambda = 0.75, 0.25$ ) slopes, indicating that the results are caused by the specific model conditions and not any

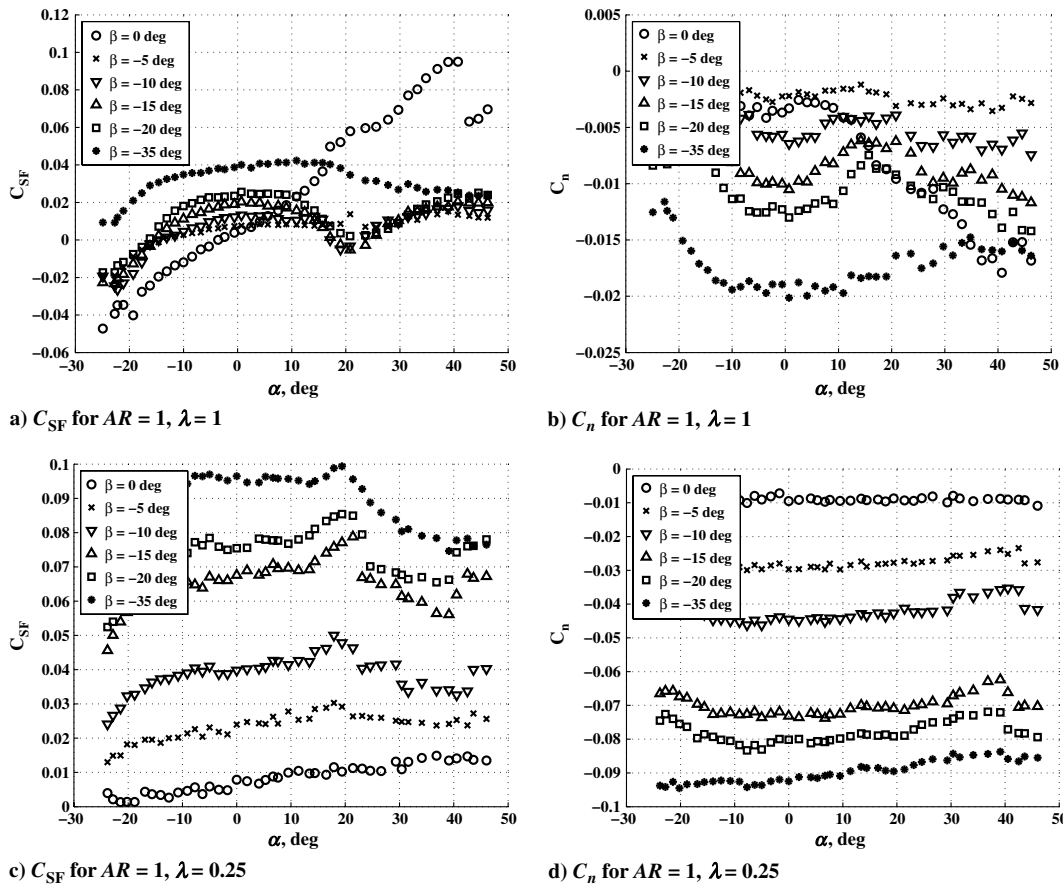
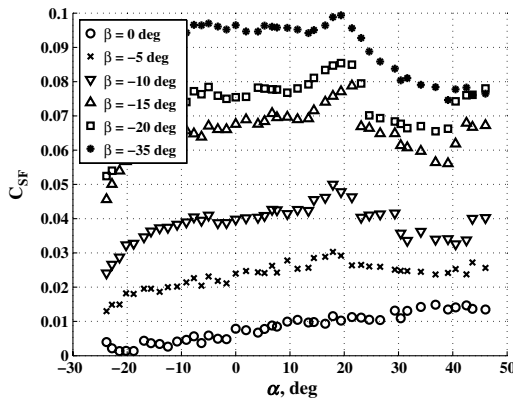
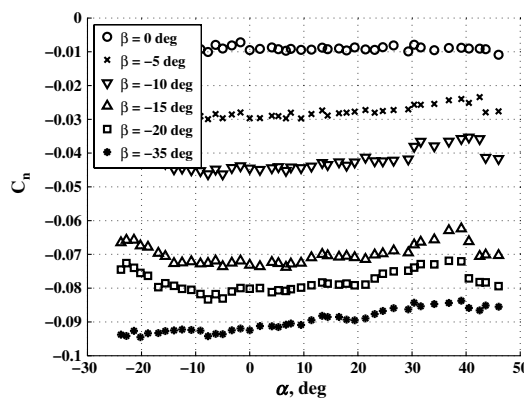
a)  $C_{SF}$  for  $AR = 1$ ,  $\lambda = 1$ b)  $C_n$  for  $AR = 1$ ,  $\lambda = 1$ c)  $C_{SF}$  for  $AR = 1$ ,  $\lambda = 0.25$ d)  $C_n$  for  $AR = 1$ ,  $\lambda = 0.25$ 

Fig. 10 Side force ( $C_{SF}$ ) and yaw moment ( $C_n$ ) coefficients for selected flat-plate wings in sideslip at  $Re = 7.5 \times 10^4$ .

potential flow inhomogeneity in the test section. This was confirmed by running a second series of tests with the model mounted upside down, in which the slopes were subsequently reversed. This result indicates the complexity of the competing effects of the flowfield associated with LAR wings, particularly at an aspect ratio of unity in which there is significant interaction between the LEV and the tip vortices.

#### D. Side Force and Yaw Moment

The results of the previous sections show the significance of the roll moment at increasing angles of attack and sideslip. The remaining lateral loads to be considered are the side force and yaw moment, both of which are related to the induced drag for the flat-plate wings and are typically smaller than the other aerodynamic loads. A selection of results for wings of  $AR = 1$  with  $\lambda = 1$  and  $0.25$  are displayed in Fig. 10 for illustrative purposes. Side force is measured in the body-centered coordinate system and thus is different from the cross-wind force. Although the magnitudes of the force and moments coefficients are small at all angles tested (as seen in Fig. 10a, the side force is less than the load created by the leading-edge imperfections at  $\beta = 0$  deg unlike the roll moments in Figs. 6 and 8), it is also clear that the trends exhibited by the loads are similar for both models. It can be seen that increasing the sideslip angle results in greater side force and yaw moment coefficients, although for the  $AR = 1$  case, the former tends toward zero at angles of attack above  $\alpha = 15$  deg. The side force is a byproduct of the induced drag created by the attached upstream tip vortex, which has a component acting in the  $+y_b$  direction of the wing. The reduction in magnitude at higher angles of attack corresponds to the roll stall region seen in Fig. 6; as the tip vortex is disrupted by the adverse pressure gradient, the reduced strength of the vortex diminishes its contribution to the induced drag and thus the side force. The only case in which this reduction does not occur is for  $\beta = 0$  deg, where the side force creation is more affected by the asymmetric separation along the leading edge. A similar trend is observed to a lesser extent for the

$\lambda = 0.25$  case in Fig. 10c, where the impact of the tip vortex and its associated induced drag are limited by the reduced wing geometry downstream of the wing tip, as seen in Fig. 5f.

The data for the yaw moment shows the influence of both aspect ratio and planform geometry. The  $AR = 3$  case (not included here) shows scattered data with coefficients on the order of  $C_n \sim 0.001$  and no meaningful differences between the different yaw angles. The magnitude of the data for the  $AR = 1$  case is somewhat larger and closer to the magnitude of  $C_l$  ( $C_n \sim 0.01$ ) and is seen to increase with sideslip angle; this trend continues for the tapered wing, although the yaw moment is seen to remain nearly constant over all angles of attack for a given sideslip angle. Again, the difference between the rectangular and tapered case can be attributed to the effects of the upstream tip vortex, which is reduced for the case of  $\lambda = 0.25$ . It is also interesting to note that, although the side force is predominantly positive, the yaw moment is nearly always negative. Both are attributed to the component of the induced drag created by the upstream tip vortex; as the vortex extends further inboard along the wing near the trailing edge (as seen in Fig. 4), a greater net side force exists on the downstream portion of the wing and creates a negative yaw moment.

## IV. Discussion

The data presented in Sec. III exhibit several interesting properties. Although the magnitudes of the coefficients are smaller than  $C_{L,max}$ , for example, the low moments of inertia of MAVs (particularly about the roll axis [3]) suggest that these loads may have a significant impact on the lateral dynamics of LAR flyers. These results are important because minimal data are available concerning the lateral loads for MAV-type wings. To develop an efficient control law for LAR vehicles at low Reynolds numbers, an accurate understanding of the load dependencies of the vehicle is necessary. It is beyond the scope of this paper to fully categorize the stability response of these wings because the rotary rate derivatives have not been measured;

**Table 2** Values of  $C_{l,\beta}$  for various planform geometries and trim angles

AR	$\lambda$	$\alpha = 5$ deg	$\alpha = 10$ deg	$\alpha = 15$ deg	$\alpha = 20$ deg
0.75	1	-0.062	-0.106	-0.161	-0.233
1	1	-0.101	-0.167	-0.238	-0.313
1.5	1	-0.053	-0.086	-0.123	-0.177
3	1	-0.019	-0.048	-0.105	-0.179
1	0.75	-0.047	-0.086	-0.150	-0.173
1	0.5	-0.057	-0.088	-0.105	-0.128
1	0.25	-0.036	-0.055	-0.067	-0.051

**Table 3** Values of  $C_{n,\beta}$  for various planform geometries and trim angles

AR	$\lambda$	$\alpha = 5$ deg	$\alpha = 10$ deg	$\alpha = 15$ deg	$\alpha = 20$ deg
0.75	1	0.125	0.113	0.099	0.093
1	1	0.038	0.031	0.022	0.028
1.5	1	0.037	0.032	0.024	0.021
3	1	0.014	0.0038	0.0018	0.0027
1	0.75	0.043	0.035	0.027	0.033
1	0.5	0.074	0.068	0.068	0.065
1	0.25	0.214	0.210	0.207	0.211

however, the static derivatives provide significant insight into the relevant control parameters for MAV flight.

### A. Stability Derivative Estimates

The data in Figs. 6–10 can be used to estimate the stability derivatives  $C_{l,\beta}$ ,  $C_{n,\beta}$ , and  $C_{SF,\beta}$  by collecting the data at a given angle of attack over a range of sideslip angles. A MAV typically flies at an angle of attack of  $\alpha \sim 10$  deg [3,5]; the derivatives were computed at  $\alpha = 5, 10, 15,$  and  $20$  deg as a realistic range of flight angles (results for 0 deg were nominally zero). The results for  $C_{l,\beta}$  and  $C_{n,\beta}$  are presented in Tables 2 and 3 (after converting the angles to radians);  $C_{SF,\beta}$  had magnitudes similar to  $C_{n,\beta}$  but is not included here for brevity.

It can be seen from the results provided that the magnitude of  $C_{l,\beta}$  is typically higher than  $C_{n,\beta}$ , although it should be noted that there are several cases in which the magnitudes of the respective derivatives are much closer. Specifically, for the taper ratio  $\lambda = 0.25$ , in which the impact of the upstream tip vortex is limited by the geometry of the tapered wing, the yaw stiffness is actually greater than the roll-stability derivative. Thus, although roll stability appears to be the parameter most influenced by sideslip, this is not a universal result for all conceivable MAV planforms. This indicates the challenges inherent to MAV design as the unique flow phenomena associated with LAR wings at low Reynolds numbers cannot be easily predicted even with geometrically similar planforms. It should still be noted that the most significant impact of roll stall from a vehicle-control perspective is in roll because this axis will almost universally have the smallest moments of inertia [3] and thus will be subjected to the highest angular accelerations for a given magnitude of the applied moment.

### B. Impact of $C_{l,\beta}$ on Vehicle Control

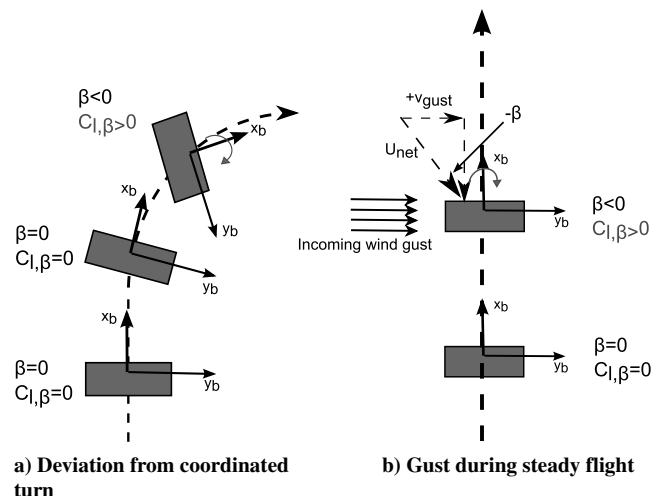
Perhaps the most significant result of the Sec. IV.A is the presence of any lateral derivatives, especially  $C_{l,\beta}$ ; this is particularly interesting because conventional aircraft stability theory predicts that a pure sideslip perturbation will not create a roll moment. An aircraft in sideslip produces a roll moment due to the lift vector of the vertical tail, the sweep and dihedral angles of the wing, the rotational inertia and slipstream of the propeller, and wing-body interference [32,38]. None of these geometric components are present for the rectangular wings, and only the wing sweep is present for the tapered wing, yet the roll-stability derivative is nonzero. Textbooks on aircraft dynamics indicate that typical aircraft configurations display good handling characteristics for approximately  $-0.10 \leq C_{l,\beta} \leq 0$  [32]. The results in Table 2 are typically larger than this despite being bereft

of the usual geometric features, which create the roll-stability derivative. The significance of this derivative can be attributed to the influence of the tip vortices; additional vertical geometry (such as tail surfaces) may potentially intensify the sensitivity to sideslip perturbations and will contribute further to the instability of the vehicle. It is important to note, however, that the roll moment created by the tip vortex asymmetry (and displayed in Table 2) inherently places LAR flyers at the cusp of poor lateral performance characteristics and, to this point, has not been considered to be a factor in MAV design. This is expected to be a critical factor in design choices such as tail sizing for the purpose of producing a passively stable aircraft.

To describe how the tip vortex-augmented roll-stability derivative could conceivably affect MAV flight dynamics, consider the diagrams shown in Fig. 11. Two distinct flight conditions are portrayed, which correspond to the test environment of this investigation; specifically, positive angle of attack and negative sideslip. Figure 11a shows a LAR wing making a coordinated turn to the right, and Fig. 11b shows a LAR wing flying at cruise and being impacted by a gust moving in the  $+y_b$  direction. The reader is reminded that, by convention, positive sideslip is defined as the  $y_b$  component of the aircraft velocity that is positive; thus, when the fluid velocity has a component in the positive  $y_b$  direction, the associated aircraft sideslip is negative.

A steady, coordinated turn is defined as a curved flight pattern with a constant bank angle and no net side force; essentially, the aircraft turns smoothly at a constant radius from the center of the turn with no sideslip [32]. This maneuver is typically actuated by using ailerons to set the bank angle and turn radius and the rudder to eliminate any side force and thus coordinate the turn (assuming it is a level turn with no altitude variation) [32]. In an ideal case, a coordinated turn has no sideslip angle and thus the roll-stability derivative should have no effect; however, a slight deviation from the  $\beta = 0$  deg case (i.e., caused by an overcompensation of the rudder) will have the effect of disrupting the tip vortex on the inboard wing tip as seen in this investigation. The  $C_{l,\beta}$  derivative created by the tip vortex asymmetry will thus contribute to a positive roll moment for a vehicle already flying with a high positive bank angle, which can be detrimental to the lateral stability of the MAV. From this concept, it is clear that the low aspect ratios of MAV wings and the associated flow behavior can significantly disrupt the maneuvering capabilities of the vehicle.

Figure 11b depicts a very different flight situation in which the desired flight path is a simple cruise condition of constant angle of attack and zero bank or sideslip angle. Should the MAV experience a gust of wind moving in the  $+y_b$  direction to create a negative sideslip angle, the tip vortex on the right wing will be convected away from the wing and the contribution of the left tip vortex to  $C_{l,\beta}$  will create a moment on the wing. This roll/yaw coupling is a contributor to the jittery nature of MAV flight, even in flight conditions with only small

**Fig. 11** Impact of  $C_{l,\beta}$  on different flight conditions for LAR wings.



gust perturbations, which would typically not be expected to induce a roll moment.

It has been acknowledged for some time that the roll-stability derivative is an underlying cause of gust instability, and some work has been done to design higher-aspect-ratio aircraft with configurations that are insensitive to lateral velocity perturbations due to near-zero magnitudes of  $C_{l,\beta}$  [41,42]. This was accomplished by adding anhedral to the wings [41] or by requiring symmetry about the  $x$ - $y$  plane [42]. The results of this investigation show that, for MAVs with aspect ratios on the order of unity, such alterations to the aircraft geometry will be ineffective in eliminating the roll-stability derivative because the inherent flow properties derived from the tip vortex asymmetry will still create roll moments during a sideslip perturbation. Thus, although  $C_{l,\beta}$  for higher-aspect-ratio aircraft is almost entirely dependent upon the vertical geometry of the vehicle, the small length scales associated with LAR flyers alter the dependencies of the roll-stability derivative as tip vortex effects become relevant.

## V. Conclusions

A series of rectangular and tapered flat-plate wings were tested in the Prototunnel at a Reynolds number of  $7.5 \times 10^4$  at sideslip angles of  $\beta = 0, -5, -10, -15, -20,$  and  $-35$  deg and a range of angles of attack to determine the effects of sideslip angle on the lateral loads of low-aspect-ratio wings. The roll moment was found to increase linearly in most cases until reaching angles of attack of at least  $\alpha = 20$  deg, at which point a roll stall event was observed. This behavior is not predicted by conventional aerodynamics because the flat-plate models do not include wing dihedral, a vertical tail, a propeller, a fuselage, or any other feature that could influence lateral loads with its projected area. Instead, the roll moment is created by the presence of the tip vortex on the upstream wing tip, which remains attached until high angles of attack. The spanwise asymmetric-induced velocities and the low-pressure core of the vortex are responsible for this roll moment. Furthermore, the tip vortex asymmetry contributes to the side force and yaw moment of the wings by affecting the induced drag vector. These loads show consistent trends with angles of attack and sideslip but are usually less significant than the roll moment; however, they may still be relevant when modeling the stability characteristics of micro aerial vehicles (MAVs). Using the data to measure the stability derivatives  $C_{l,\beta}$  and  $C_{n,\beta}$  showed the roll-stability derivative to typically be larger than the yaw stiffness and often higher than values widely recognized as characteristic of "good handling" aircraft. The effect of this significant  $C_{l,\beta}$  value can result in lateral instabilities in flight conditions such as coordinated turns and gusty environments, which corresponds with observations made during MAV flight testing. The values of the lateral derivatives of these flat-plate wings (particularly  $C_{l,\beta}$ ) inherently place MAVs on the brink of passive instability, which would be exacerbated by even minor design flaws in dihedral or vertical tail sizing. The data in this paper show the unique and poorly understood dependencies of MAV aerodynamic loads on flow phenomena such as the tip vortex, which must be accounted for in an accurate model for flight control of a MAV.

## References

- [1] Grasmeyer, J., and Keennon, M., "Development of the Black Widow Micro Air Vehicle," *39th AIAA Aerospace Sciences Meeting and Exhibit*, AIAA Paper 2001-0127, 2001.
- [2] Hundley, R., and Gritton, E., "Future Technology-Driven Revolutions in Military Operations," RAND Corp., Rept. DB-110-ARPA, Santa Monica, CA, 1994.
- [3] Wasak, R., Jenkins, D., and Ifju, P., "Stability and Control Properties of an Aeroelastic Fixed Wing Micro Aerial Vehicle," *AIAA Atmospheric Flight Mechanics Conference and Exhibit*, AIAA Paper 2002-4005, 2001.
- [4] Ifju, P., Jenkins, D., Ettinger, S., Lian, Y., Shyy, W., and Waszak, M., "Flexible-Wing-Based Micro Air Vehicles," *40th Aerospace Sciences Meeting and Exhibit*, AIAA Paper 2002-0705, Jan. 2002.
- [5] Shields, M., and Mohseni, K., "Static Aerodynamic Loading and Stability Considerations for a Micro Aerial Vehicle," *28th AIAA Applied Aerodynamics Conference*, AIAA Paper 2010-4389, June–July 2010.
- [6] Spedding, G., and McArthur, J., "Span Efficiencies of Wings at Low Reynolds Numbers," *Journal of Aircraft*, Vol. 47, No. 1, 2010, pp. 120–128.  
doi:10.2514/1.44247
- [7] Arena, A., and Mueller, T., "Laminar Separation, Transition, and Turbulent Reattachment near the Leading Edge of Airfoils," *AIAA Journal*, Vol. 18, No. 5, 1980, pp. 747–753.  
doi:10.2514/3.50815
- [8] Brendel, M., and Mueller, T., "Boundary-Layer Measurements on an Airfoil at Low Reynolds Numbers," *Journal of Aircraft*, Vol. 25, No. 7, 1988, pp. 612–617.  
doi:10.2514/3.45631
- [9] Mueller, T., and Delaurier, J., "Aerodynamics of Small Vehicles," *Annual Review of Fluid Mechanics*, Vol. 35, 2003, pp. 89–111.  
doi:10.1146/annurev.fluid.35.101101.161102
- [10] Shyy, W., Lian, Y., Tang, J., Viieru, D., and Liu, H., *Aerodynamics of Low Reynolds Number Flyers*, Cambridge Aerospace Series, Cambridge Univ. Press, New York, 2008, pp. 29–62.
- [11] Lambourne, N., and Bryer, D., "Some Measurements in the Vortex Flow Generated by a Sharp Leading-Edge Having 65 Degrees Sweep," Aeronautical Research Council TR-477, London, 1959.
- [12] Earnshaw, P., "An Experimental Investigation of the Structure of a Leading Edge Vortex," Aeronautical Research Council TR-3281, London, 1961.
- [13] Payne, F., Ng, T., Nelson, R., and Schiff, L., "Visualization and Wake Surveys of Vortical Flows Over a Delta Wing," *AIAA Journal*, Vol. 26, No. 2, 1988, pp. 137–143.  
doi:10.2514/3.9864
- [14] Taira, K., and Colonius, T., "Three-Dimensional Flows Around Low-Aspect-Ratio Flat-Plate Wings at Low Reynolds Numbers," *Journal of Fluid Mechanics*, Vol. 623, 2009, pp. 187–207.  
doi:10.1017/S0022112008005314
- [15] Swanton, E., Vanier, B., and Mohseni, K., "Flow Visualization and Wall Shear Stress of a Flapping Model Hummingbird Wing," *Experiments in Fluids*, Vol. 49, No. 3, 2010, pp. 657–671.  
doi:10.1007/s00348-010-0832-1
- [16] Miao, J., Kuo, K., Liu, W., Hsieh, S., Chou, J., and Lin, C., "Flow Developments Above 50-Degree Sweep Delta Wings with Different Leading Edge Profiles," *Journal of Aircraft*, Vol. 32, No. 4, 1995, pp. 787–796.  
doi:10.2514/3.46792
- [17] Williams, D., Quach, V., Kerstens, W., Buntain, S., Tadmor, G., Rowley, C., and Colonius, T., "Low-Reynolds Number Wing Response to an Oscillating Freestream with and Without Feed Forward Control," *47th AIAA Aerospace Sciences Meeting*, AIAA Paper 2009-0143, 2009.
- [18] Williams, D., Tadmor, G., Colonius, T., Kerstens, W., Quach, V., and Buntain, S., "Lift Response of a Stalled Wing to Pulsatile Disturbances," *AIAA Journal*, Vol. 47, No. 12, 2009, pp. 3031–3037.  
doi:10.2514/1.45407
- [19] Hall, M., "A Theory for the Core of a Leading-Edge Vortex," *Journal of Fluid Mechanics*, Vol. 11, 1961, pp. 209–228.  
doi:10.1017/S0022112061000470
- [20] Polhamus, E., "Application of the Leading-Edge-Suction Analogy of Vortex Lift to the Drag Due to Lift of Sharp-Edge Delta Wings," NASA TN-D-4739, Aug. 1968.
- [21] Pelletier, A., and Mueller, T., "Low Reynolds Number Aerodynamics of Low-Aspect-Ratio, Thin/Flat/Cambered-Plate Wings," *Journal of Aircraft*, Vol. 37, No. 5, 2000, pp. 825–832.  
doi:10.2514/2.2676
- [22] Torres, G., and Mueller, T., "Low-Aspect-Ratio Wing Aerodynamics at Low Reynolds Numbers," *AIAA Journal*, Vol. 42, No. 5, 2004, pp. 865–873.  
doi:10.2514/1.439
- [23] Shields, M., and Mohseni, K., "Effects of Sideslip on the Aerodynamics of Low-Aspect-Ratio Low-Reynolds-Number Wings," *AIAA Journal*, Vol. 50, No. 1, 2012, pp. 85–99.  
doi:10.2514/1.J051151
- [24] Lam, K., and Leung, M., "Asymmetric Vortex Shedding Flow Past an Inclined Flat Plate at High Incidence," *European Journal of Mechanics — B/Fluids*, Vol. 24, No. 1, 2005, pp. 33–48.  
doi:10.1016/j.euromechflu.2004.05.004
- [25] Jian, T., and Ke-Qin, Z., "Numerical and Experimental Study of Flow Structure of Low Aspect Ratio Wing," *Journal of Aircraft*, Vol. 41, No. 5, 2004, pp. 1196–1201.  
doi:10.2514/1.5467
- [26] Gresham, N., Wang, Z., and Gursul, I., "Low Reynolds Number Aerodynamics of Free-to-Roll Low Aspect Ratio Wings," *Experiments*

- in Fluids*, Vol. 49, 2010, pp. 11–25.  
doi:10.1007/s00348-009-0726-2
- [27] Lamar, J., “Prediction of Vortex Flow Characteristics of Wings at Subsonic and Supersonic Speeds,” *Journal of Aircraft*, Vol. 13, No. 7, 1975, pp. 490–494.  
doi:10.2514/3.58681
- [28] Zimmerman, C., “Characteristics of Clark Y Airfoils of Small Aspect Ratios,” NACA TM-431, May 1932.
- [29] Winter, H., “Flow Phenomena on Plates and Airfoils of Short Span,” NACA TM-798, July 1936.
- [30] Selig, M., Guglielmo, J., Broeren, A., and Giguere, P., *Summary of Low Speed Airfoil Data*, Vol. 1, SoarTech Publ., Virginia Beach, VA, 1995, pp. 7–14, 53–245.
- [31] Shields, M., and Mohseni, K., “Experimental Complications Inherent to Low Reynolds Number Wind Tunnel Testing,” *49th AIAA Aerospace Sciences Meeting*, AIAA Paper 2011-0873, Jan. 2011.
- [32] Phillips, W., *Mechanics of Flight*, 2nd ed., Wiley, New York, 2010, pp. 319–323, 499–597.
- [33] Colonius, T., and Williams, D., “Control of Vortex Shedding on Two- and Three-Dimensional Airfoils,” *Philosophical Transactions of the Royal Society A*, Vol. 369, 2011, pp. 1525–1539.  
doi:10.1098/rsta.2010.0355
- [34] “Calibration and Use of Internal Strain-Gage Balances with Application to Wind Tunnel Testing,” AIAA, Recommended Practice R-091-2003, Reston, VA, 2003.
- [35] Rae, W., and Pope, A., *Low-Speed Wind Tunnel Testing*, 2nd ed., Wiley, New York, 1984, pp. 300–378.
- [36] Bendat, J., and Piersol, A., *Random Data: Analysis and Measurement Procedures*, 4th ed., Wiley Series in Probability and Statistics, Wiley, Hoboken, New Jersey, 2011, pp. 249–355.
- [37] Hall, M., “Vortex Breakdown,” *Annual Review of Fluid Mechanics*, Vol. 4, 1972, pp. 195–218.  
doi:10.1146/annurev.fl.04.010172.001211
- [38] Schmidt, L., *Introduction to Aircraft Flight Dynamics*, AIAA, Reston, VA, 1998, pp. 29–42.
- [39] Prandtl, L., “Applications of Modern Hydrodynamics to Aeronautics,” NACA TR-116, 1923.
- [40] Bastedo, W., and Mueller, T., “Spanwise Variation of Laminar Separation Bubbles on Wings at Low Reynolds Numbers,” *Journal of Aircraft*, Vol. 23, No. 9, 1986, pp. 687–694.  
doi:10.2514/3.45363
- [41] Thomasson, P. G., “The Flight Dynamics of a Gust Insensitive Unmanned Aircraft,” *Control & Guidance of Remotely Operated Vehicles, IEE Colloquium on*, IET, June 1995, pp. 6/1–6/3.  
doi:10.1049/ic:19950802
- [42] Pisano, W. J., and Lawrence, D. A., “Autonomous Gust Insensitive Aircraft,” *AIAA Guidance, Navigation and Control Conference and Exhibit*, AIAA Paper 2008-6510, Aug. 2008.